DOI: 10.13009/EUCASS2023-418
Aerospace Europe Conference 2023 – 10TH EUCASS – 9TH CEAS

Influence of the Leading-Edge Radius on Vortex Development at Hybrid-Delta-Wing Configurations

Dominik Sedlacek[⋆†], *Ankit Kasi*[⋆] *and Christian Breitsamter*[⋆]
[⋆]*Chair of Aerodynamics and Fluid Mechanics, Technical University of Munich*
Boltzmannstr. 15, 85748 Garching bei München, Germany
dominik.sedlacek@tum.de
[†]Corresponding author

Abstract

This study investigates the influence of the leading-edge radius on vortex systems at hybrid-delta-wing configurations through wind tunnel experiments and simulations. Two variants with different leading-edge radii are compared to a sharp-edged configuration. The results show similar vortex development with respect to a strake and main wing vortex at various angles of attack for both configurations. The double-delta-wing configuration exhibits a more stable strake vortex with increasing leading-edge radius, leading to a downstream shift in vortex breakdown. The interaction between the vortices occurs more downstream, implying a weaker attraction between them. The triple-delta-wing configuration shows a lower influence of leading-edge radius, with similar flow fields among different variants. Overall, the study highlights the sensitivity of the vortex system to changes in leading-edge radius.The triple-delta-wing configuration is associated with enhanced lateral stability characteristics compared to the double-delta-wing configuration.

1. Introduction

Highly agile aircraft often operate under extreme flight conditions, necessitating effective supersonic cruise capabilities and high maneuverability at subsonic conditions [1]. Such configurations typically feature low-aspect-ratio wings with medium to high sweep angles and small leading-edge radii. At these wing planforms, the flow tends to separate near the leading edges and thus leading-edge vortices are formed already at low angles of attack. These vortices induce suction peaks on the wing surface, leading to a nonlinear increase in lift. As the angle of attack increases, the fully developed leading-edge vortices undergoes breakdown, causing the vortex cross-section to expand and a transient flow field to extend downstream of the breakdown location. With further increase in the angle of attack, the breakdown location moves upstream [2]. Within the wake of the vortex breakdown, quasi-periodic velocity oscillations emerge due to helical mode instabilities. For slender wings with leading-edge sweep angles, φ, greater than 60°, the vortex core exhibits a jet-like structure and the breakdown is abrupt owing to a pronounced adverse pressure rise [3]. The vortex breakdown is characterized by reverse flow and significantly affects the flight stability characteristics. In the case of non-slender and semi-slender wings with leading-edge sweep angles of $50^\circ < \varphi < 60^\circ$, the vortex core transitions to a wake-like structure at moderate angles of attack. The vortex breakdown at this type of wing planform manifests as a gradual transition with a less abrupt expansion of the vortex core and a moderate adverse pressure gradient [4]. Due to the smoother breakdown, flight stability characteristics exhibit a more stable behavior for non-slender wing planforms.

Configurations featuring multiple-swept leading edges exhibit a significantly more complex flow field. Different swept leading-edge sections lead to the development of multiple vortices, forming a vortex system. In double-delta-wing configurations, two vortices form at small angles of attack and remain adjacent until the trailing edge. As the angle of attack increases, these vortices merge and start rotating around each other. Upon further increase in the angle of attack, the merged vortices burst. The behavior of the vortices is strongly influenced by the leading-edge sweeps and the position of the transition between different swept leading-edge sections [5].

At the Chair of Aerodynamics and Fluid Mechanics at the Technical University of Munich (TUM-AER), several investigations regarding the flow field and flight stability characteristics of double- and triple-delta-wing configurations, which bear a resemblance to the configurations examined in this study [6, 7, 8]. The investigations revealed that the inboard vortex (IBV) dominates the breakdown characteristics, exhibiting different abruptness for non-slender and slender wing planforms. The midboard vortex (MBV), which develops in the midboard section, is strongly influenced by the behavior of the IBV. In comparison to the slender, double-delta-wing configuration, the non-slender, triple-delta-wing configuration displays smoother onset of instabilities and smaller magnitudes of instability [9].

DOI: 10.13009/EUCASS2023-418

To enhance the understanding of vortex formation, interaction, and bursting, it is crucial to employ Computational Fluid Dynamics (CFD) simulations, an emerging solution investigating vortex flows and their effects. Over time, numerical analysis of delta wings has become increasingly accurate. Morton studied the flow field of a delta wing with a sweep angle of 70° using Detached Eddy Simulation (DES) and Reynolds-Averaged Navier-Stokes (RANS) methods. The DES, employing an unstructured mesh with 2.47×10^6 cells, exhibited good agreement with experimental data. The RANS solution utilizing the one-equation Spalart-Allmaras (SA) turbulence model [10] encountered challenges in capturing vortex bursting features. However, incorporating a Rotation Correction (RC) [11] led to an improved agreement with experimental data, particularly in the vortex breakdown region [12].

Luckring et al. performed simulations to analyze the flow field of the F-16XL aircraft, which bears a resemblance to the triple-delta-wing configuration investigated in the present study. The turbulence models considered included the one-equation Spalart–Allmaras turbulence model with and without RC, as well as the k-ω model. All models yielded similar results for pressure distribution and exhibited good agreement with flight test measurements. However, for non-slender wing planforms, challenges arise in accurately characterizing separation, leading-edge vortex formation, and vortex breakdown behavior [13]. Sedlacek et al. [7] conduct a grid convergence study and a comparison of different numerical methods is discussed. Although the delayed detached eddy simulation (DDES) results show a better agreement with the experimental results, the URANS results are in good agreement with the experimental data and exhibit a significantly higher efficiency.

Luckring [14] shows the influence of the leading-edge radius (LER) on delta wings at different inflow conditions. A blunt leading edge increases the number of parameters influencing the vortex origin, the vortex properties, and therefore, the stability characteristics by the leading-edge radius. The flow at the sharp-edged wing separates directly at the leading edge. For the wing with a blunt leading edge, the flow is attached in the most upstream cross-section and a vortex suction peak is visible at 60% root chord. With an increase in LER, the sensitivity to Reynolds number effects is increasing and the Reynolds number is a further important parameter developing of the vortex systems.

In this study, the influence of the LER is compared by employing experimental force and moment data and by CFD flow field analysis. The flow field discussions regarding the wing planforms with a sharp leading edge are published by Pfnür [6] and Sedlacek [7, 8]. Therefore, a round LE is implemented for the existing wing planforms, a double- and a triple-delta-wing configuration. The LER is set to $r_N/c_r = 0.0025$ and $r_N/c_r = 0.005$. The objective is to analyze and comprehend the influence of the LER on different multiple-delta-wing planforms. The force and moment characteristics and the flow field will be discussed at varying angles of attack and at symmetric, $\beta = 0°$, and asymmetric inflow conditions with an angle of sideslip of $\beta = 5°$.

2. Configurations

This study investigates a generic wing-fuselage configuration with interchangeable wing planforms. This configuration is developed in collaboration with Airbus Defence and Space (Airbus DS). The focus is on two specific configurations, referred to as NA1 W2 and NA1 W1, as illustrated in Fig. 1.

NA1 W2, see Fig. 1a, is a double-delta-wing configuration characterized by a high leading-edge sweep angle $\varphi_2 = 75°$ in the front part (strake) and a rear wing section with a medium leading-edge sweep angle $\varphi_3 = 52.5°$. The wings in both configurations consist of flat plates with sharp leading edges. On the other hand, NA1 W1, cf. Fig. 1b, is a triple-delta-wing configuration comprising three wing segments with different leading-edge sweeps. The front section, the so-called leading-edge vortex controller (LEVCON), has a medium leading-edge sweep angle of $\varphi_1 = 52.5°$, followed by a strake section with a high leading-edge sweep angle of $\varphi_2 = 75°$, and the main wing section has a similar leading-edge sweep angle as the front section, $\varphi_1 = \varphi_3$.

As previously mentioned, there are three leading-edge sets for each configuration, sharp (LER00), small radius (LER02), and large radius (LER04). Figure 1a shows the wing's leading edge. The LER is chosen as $r_N/c_r = 0.0025$ or $r_N = 2\,mm$ for the small radius and $r_N/c_r = 0.005$, $r_N = 4\,mm$ for the large radius.

The essential geometric parameters of the two configurations are summarized in Table 1 [9].

3. Numerical Methods and Grid

The main points on the set-up of the computational grid and numerical parameters are given in the following.

3.1 Grid

The grid shown in Fig. 2 was generated using the Centaursoft grid generator, following the guidelines outlined by Cummings et al. [15]. The aim was to create a similar grid structure for all configurations. The surface grid, responsible

DOI: 10.13009/EUCASS2023-418

Table 1: Geometrical parameters of the NA1 W2 and NA1 W1 configurations.

		NA1 W2	NA1 W1
c_r	$[m]$	0.802	0.802
s	$[m]$	0.367	0.417
S_{Ref}	$[m^2]$	0.266	0.329
Λ	–	0.16	0.15
l_μ	$[m]$	0.426	0.468
l_1/c_r	–	–	0.125
l_2/c_r	–	0.475	0.350
l_3/c_r	–	0.475	0.475
φ_1	°	–	52.5
φ_2	°	75	75
φ_3	°	52.5	52.5

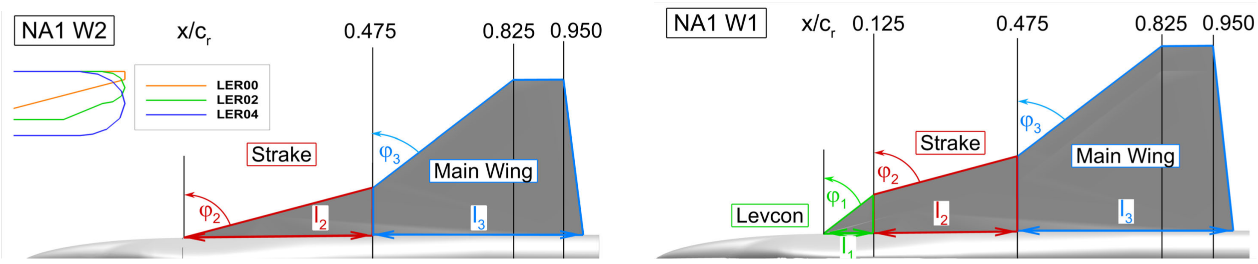

(a) NA1 W2

(b) NA1 W1

Figure 1: Wing planforms.

for resolving the wall boundary layer, consists of triangular elements. The farfield region, representing the outer frame of the grid, was chosen to be sufficiently large with a diameter of 50 times the model's size to minimize the influence of farfield boundary conditions on the flow around the model.

To accurately capture the wall boundary layer, the prism layer on the surface has an unstructured character, while it has a structured character normal to the surface. The height of the prism layer is determined by the number of layers, which is set to $n_{Prism} = 33$, and a stretching ratio of 1.25. These specifications are further refined in critical areas. The primary cell shape used is an unstructured tetrahedron grid, which connects directly to the prism layer and fills the space enclosed by the farfield, plane of symmetry, and the model. To improve the resolution of the vortex system, a block of structured hexahedral elements is inserted above the wing. Pyramids are used to connect the hexahedral block to the tetrahedron grid.

The grid is additionally refined in specific areas, such as the leading edge and the vortex field. The spacing near the wing's surface is such that the distance in wall units, represented by y^+, is less than 1.0, except in a small region near the wing root. A grid independence study and the validation of CFD results comparing force and moment coefficients and cross flow velocity fields with experimental data is shown by Sedlacek et al. [7].

3.2 Numerical Setup

The incompressible Navier-Stokes equations are solved for the flow simulations using the DLR-Tau-Code, employing a finite volume method. Unsteady Reynolds-Averaged Navier-Stokes (URANS) is the used numerical method.

In the URANS approach, turbulence is modeled using the one-equation Spalart-Allmaras model with rotation correction [16, 17, 10]. The equations are solved using a lower-upper symmetric Gauss-Seidel scheme. The unsteady time step $\delta_t = 2 \times 10^{-4}$ s is calculated based on a characteristic time step value of $\delta_t^* = 0.002$ s recommended in the literature [18], see Equation 1. The time stepping is employed with the Backward Euler scheme. The number of inner iterations per time step is limited to 50-300.

$$\delta_t = \frac{\delta_t^* \cdot l_\mu}{U_\infty} \tag{1}$$

A second-order central scheme as a discretization type with matrix dissipation was employed. The results of the converged URANS solutions are presented in this study. The shown results represent the averaged values of the

DOI: 10.13009/EUCASS2023-418

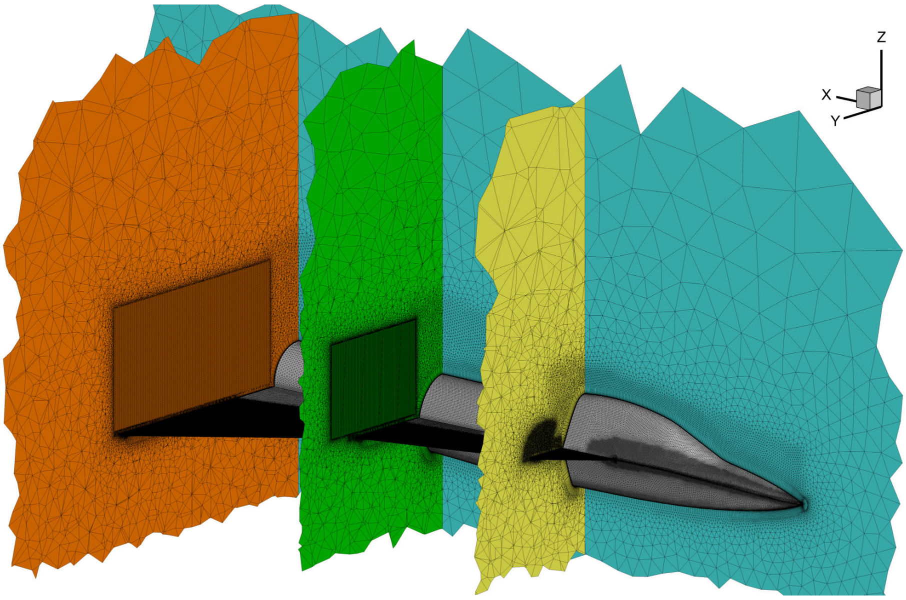

Figure 2: Overview of the grid structure for NA1 W1 [7].

flow field. The graphs and figures presented in the following survey refer to the mean values of the time-accurate CFD computations. The cauchy convergence control is applied with control variables specified as lift coefficient, drag cofficient, pitching moment coefficient, and the maximum nondimensional eddy viscosity. The convergence criterion is reached if the fluctuations of one of these variables are below 10^{-4} for more than 25 inner iterations per time step.

4. Experimental Methods

The experiments were conducted in Wind Tunnel A at the Chair of Aerodynamics and Fluid Mechanics of the Technical University of Munich. The wind tunnel has an open test section with dimensions of $1.80\,m \times 2.40\,m$ and a length of $4.80\,m$. It is capable of reaching a maximum velocity of $U_{WT} = 65\,m/s$ and provides a turbulence level below 0.4%.

To control the model's orientation, a three-component model support was used, allowing adjustment of the angle of attack α, angle of sideslip β, and roll angle γ. The support can be adjusted for sideslip and roll angles within ±90°, while the angle of attack is limited to 0° to 40°.

For the measurements, a freestream velocity of $U_\infty \approx 50\,m/s$ and a Reynolds number of $Re = 3.0 \times 10^6$ based on the reference length $l_{Re} = 1\,m$ were used. An internal six-component strain-gauge balance was utilized to measure the aerodynamic forces and moments. The maximum sustainable loads were $900\,N$ for axial forces, $450\,N$ for lateral forces, and $2500\,N$ for normal forces. The maximum sustainable moments were $120\,Nm$ for rolling moments, $160\,Nm$ for pitching moments, and $120\,Nm$ for yawing moments. The forces and moments were measured with a sampling frequency of $f_m = 800\,Hz$ and the total acquisition time was $t_m = 5\,s$. The accuracy of the aerodynamic coefficients for the specific test setup is presented in Table 2 with respect to repeatability.

Table 2: Repeatability of measured force and moment coefficients.

ΔC_D	ΔC_Y	ΔC_L	ΔC_{mx}	ΔC_{my}	ΔC_{mz}
±0.0035	±0.0012	±0.0051	±0.0005	±0.0017	±0.00042

Repeatability is related to the standard deviation of the coefficients determined from multiple angle-of-attack polar measurements. The standard deviation was calculated for each angle of attack and coefficient. The force and moment measurements presented in the subsequent analysis refer to the mean values obtained from the series of measurements for each angle of attack.

5. Flow Field Analysis

This study analyzes the influence of the leading-edge radius on the vortex systems at multiple-swept leading edges using the flow field, vortex core characteristics, and near-wall flow. The flow field for the double-delta-wing configuration

DOI: 10.13009/EUCASS2023-418

is shown in Fig. 3 by means of an isosurface of 2% pressure loss $(p_t - p_{t,\infty})/p_{t,\infty}$ colored by the nondimensional axial velocity u/U_∞ for three angles of attack $\alpha = \{16°, 24°, 32°\}$. Black isosurfaces show an area of $u/U_\infty = 0$ and, therefore, stagnating or reversed flow. An experimental analysis of the flow field at the sharp leading edge (LER00) was conducted in Ref. [9]. For an angle of attack of $\alpha = 16°$, two vortices develop, see Figs. 3a to 3c. The vortex forming at the strake is called Inboard Vortex (IBV) and the one forming at the main wing is referred to as Midboard Vortex (MBV). The vortices exhibit high axial velocities in the core, indicated by the dark red coloring of the isosurface. The vortices interact with each other and enter into a joint, strong rotation that is directed in the downstream and outboard direction. This is also shown for the configurations with round leading edges, cf. Figs. 3b and 3c. The axial core velocities appear slightly lower, especially in the rear part of the wing, the core velocity decreases, and the isosurfaces expand with increasing LER.

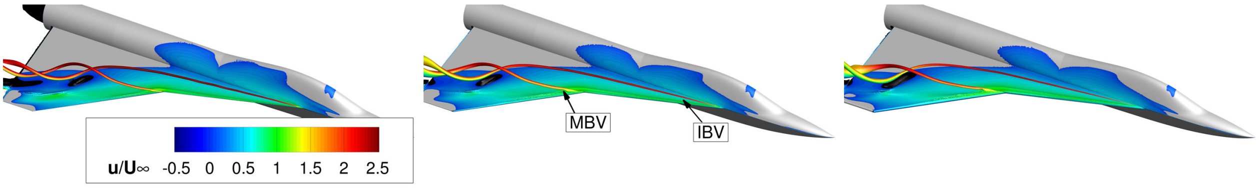

(a) LER00, $\alpha = 16°$ (b) LER02, $\alpha = 16°$ (c) LER04, $\alpha = 16°$

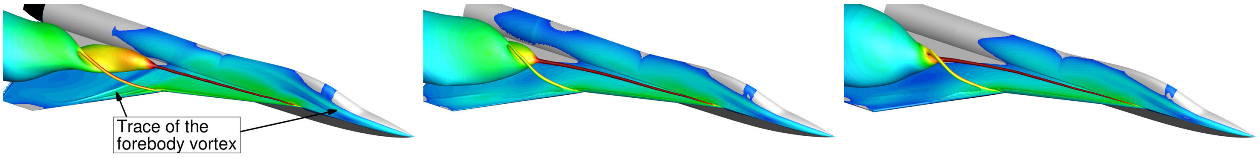

(d) LER00, $\alpha = 24°$ (e) LER02, $\alpha = 24°$ (f) LER04, $\alpha = 24°$

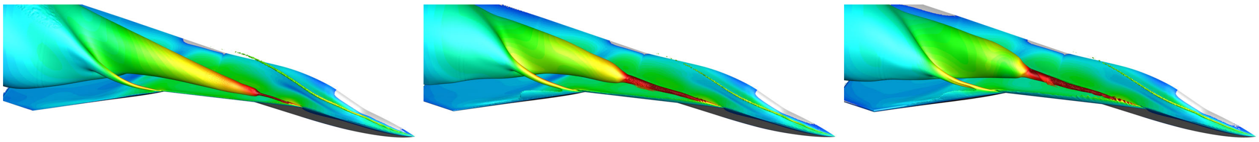

(g) LER00, $\alpha = 32°$ (h) LER02, $\alpha = 32°$ (i) LER04, $\alpha = 32°$

Figure 3: Isosurface of the pressure loss of 2% colored with the non-dimensional axial velocity for the double-delta-wing configuration with different leading-edge radii (LER00, LER02, LER04) and different angles of attack $\alpha = \{16°, 24°, 32°\}$

At an angle of attack of $\alpha = 24°$, see Figs. 3d to 3f, vortex breakdown occurs above the wing. First, the IBV bursts abruptly, indicated by a rapidly increasing diameter of the vortex core and the decrease in axial velocity. Downstream of the breakdown, the MBV interacts with the wake of the burst IBV and, after its breakdown, dissolves in the wake of the IBV. The merging of the two burst vortices leads to another increase of the wake area. This phenomenon also appears for both configurations with round leading edges. However, it is already visible that the IBV vortex bursts more downstream with increasing LER. For the LER04 configuration, cf. Fig. 3f, the IBV and MBV breakdown occurs almost simultaneously. Close observation shows a more pronounced secondary vortex at the LER00 configuration. Right below the vortex breakdown, the trace of the forebody vortex, which is pulled below the vortex system, is observable. This does not appear for the other configurations.

With a further increase in the angle of attack, $\alpha = 32°$, see Figs. 3g to 3i, vortex breakdown is shifted more upstream and the wake area of the burst vortices is increasing. The downstream shift of the vortex breakdown with increasing LER is even more pronounced compared to the angle of attack of $\alpha = 24°$.

The vortex development for the triple-delta-wing configuration, see Fig. 4, differs from the vortices at the double-delta-wing configuration. The flow separates at the leading-edge-vortex controller (LEVCON). It forms a strong outboard-directed vortex which gets redirected in flow direction by the shear layer separating from the highly swept strake region. The strake shear layer encloses the vortex and feeds it with energy [9]. The isosurface with a pressure-loss of 2%, cf. Fig. 4 features a larger diameter and lower velocities compared to the double-delta-wing configuration. The interaction with the MBV is less strong and vortex breakdown occurs already at $\alpha = 16°$ above the wing, see Fig. 4a. The MBV also bursts close to the trailing edge and a large joint wake area forms downstream of

DOI: 10.13009/EUCASS2023-418

the breakdown of the vortices. The flow fields for LER00 and LER02 are quite similar. Hence, no large influence of the round leading edges can be observed at this angle of attack. The configuration with the largest LER, cf. Fig. 4c, exhibits a more stable vortex system and the MBV stays stable above the whole wing. The secondary vortex formation, which is observable close to the wing surface, is similar for all configurations at this angle of attack.

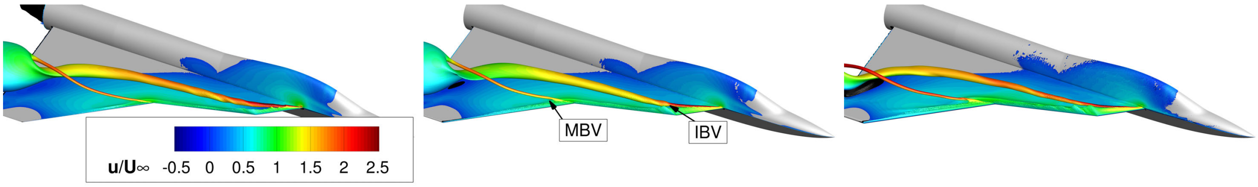

(a) LER00, $\alpha = 16°$ (b) LER02, $\alpha = 16°$ (c) LER04, $\alpha = 16°$

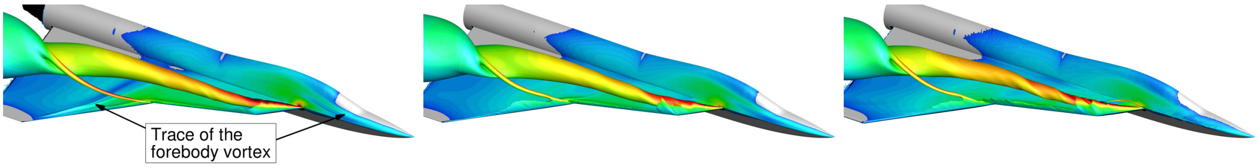

(d) LER00, $\alpha = 24°$ (e) LER02, $\alpha = 24°$ (f) LER04, $\alpha = 24°$

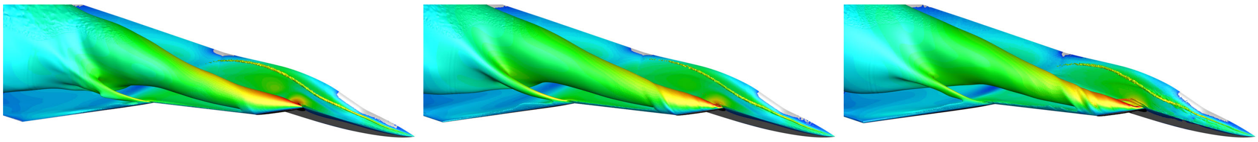

(g) LER00, $\alpha = 32°$ (h) LER02, $\alpha = 32°$ (i) LER04, $\alpha = 32°$

Figure 4: Isosurface of the pressure loss of 2% colored with the non-dimensional axial velocity for the triple-delta-wing configuration with different leading-edge radii (LER00, LER02, LER04) and different angles of attack $\alpha = \{16°, 24°, 32°\}$

At $\alpha = 24°$, the diameter of the vortex core increases and the shown velocities decrease, see Fig. 4d. This indicates vortex breakdown. With the breakdown of the MBV, a common wake area forms similar to the angle of attack $\alpha = 16°$. Comparable to the double-delta-wing configuration, the trace of the forebody vortex is observable only for the LER00 configuration. However, at this angle of attack, the flow field is quite similar for all configurations, see Figs. 4e and 4f.

The highest angle of attack, $\alpha = 32°$, features a significant increase in the diameter of the isosurface, indicating vortex breakdown close to the apex. The trace and an isosurface of the forebody vortex are observable for all configurations. Furthermore, for the LER04 configuration, even multiple smaller forebody vortices are visible close to the apex, cf. Fig. 4i.

6. Vortex Core Characteristics

In this section, the vortex core characteristics are analyzed. The vortex core is identified by an algorithm that searches for the maximum Q-criterion in jet-type vortices. The Q-criterion is a mathematical approach for identifying vortex structures in fluid flows. It defines a vortex as a connected region in the flow field where the second invariant of the velocity gradient tensor is positive. In the context of the Q-criterion, it indicates that the amount of vortex strength (associated with rotation) dominates over the amount of shear rate (associated with deformation). The Q-criterion is calculated by Kolar[19]:

$$Q = \frac{1}{2}(u_{i,i}^2 - u_{i,j}u_{j,i}) = -\frac{1}{2}u_{i,j}u_{j,i} = \frac{1}{2}(||\mathbf{\Omega}||^2 - ||\mathbf{S}||^2) > 0 \tag{2}$$

Where Ω is the vorticity tensor and S represents the strain rate tensor. A maximum level of the Q-criterion represents the jet-type vortex core. The minimum velocity magnitude determined the position of the wake-type core. Therefore, the trajectory is also shown downstream of the breakdown onset.

In Fig. 5, the core characteristics of the double-delta-wing configurations are shown. The sharp-edged variant is represented in orange, the LER02 configuration in green, and the configuration with the largest LER in blue.

DOI: 10.13009/EUCASS2023-418

Furthermore, the IBV is depicted as a solid line and the MBV as a dash-dot line. The trajectory in xy-direction is presented in Fig. 5a. The previously discussed strong interaction and rotation are observable. However, the strength of the interaction varies between the configurations though the trajectories of the vortices for all variants are similar after development. The vortices of the LER00 configuration feature the strongest interaction and with increasing LER the rotation decreases, hence the crossing of the vortices appears more downstream. This is also shown in the vortex trajectories in xz-direction, see Fig. 5b. An increase in LER leads to a lower vortex trajectory and the movement of the IBV is enhanced while the MBV exhibits a minor movement. Additionally, the MBV features a faster detachment from the wing surface for smaller/sharp LER.

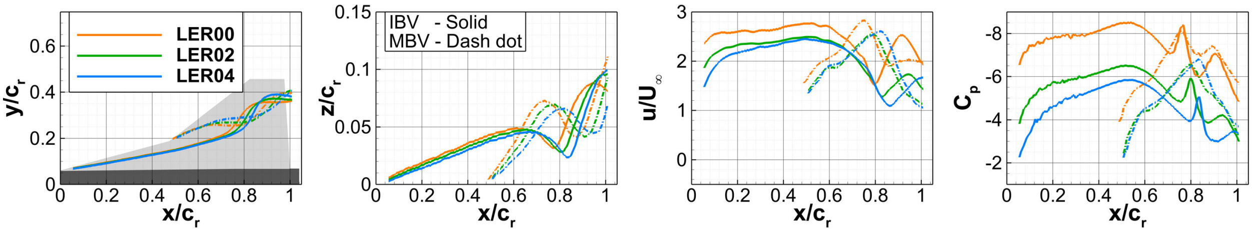

(a) y/c_r (b) z/c_r (c) u/U_∞ (d) C_p

Figure 5: Vortex core characteristics at $\alpha = 16°$ for the double-delta-wing configuration.

Figure 5c shows the nondimensional axial core velocities. The core velocities for the sharp-edged variant are significantly higher than for the round leading-edge configurations, which feature similar core velocities. However, the core velocity decreases more upstream for the configuration with the sharp leading edges. The MBV at the LER00 configuration reaches its maximum core velocity at $x/c_r \approx 0.75$. The maximum is shifted more downstream with increasing LER. Due to the stronger interaction at the LER00 configuration, the axial core velocity of the IBV increases significantly, $\Delta u/U_\infty \approx 1.0$, when starting to rotate with the MBV. The increase in the axial IBV core velocity also occurs for the configurations with round leading edges but to a minor extent (LER02: $\Delta u/U_\infty \approx 0.5$, LER04: $\Delta u/U_\infty \approx 0.55$) and is detected more downstream. In Fig. 5d, the pressure coefficient is shown. Similar to the axial velocity, the pressure levels decrease with increasing LER. Furthermore, the interaction of vortices leads to a decrease in pressure, thereby counteracting the adverse pressure gradient within the vortex core. With increasing LER, the suction peak in the core moves more downstream, depending on the delayed interaction of the vortices. The suction peak of the IBV superposes with the minimum pressure of the MBV core. This increase in velocity and core suction occurs slightly upstream of the crossing of the vortex trajectories and, therefore, in the region where the IBV is moved closer to the wing surface.

The vortex core characteristics for the triple-delta-wing configuration are shown in Fig. 6. The vortex trajectories in xy-direction, cf. Fig. 6a, exhibit less interaction for all LER variants compared to the double-delta-wing configuration. Additionally, the variants with small LER and sharp leading edge feature a similar behavior, but the LER04 configuration shows a more outboard MBV trajectory. Therefore, the crossing between the vortices occurs more downstream. Regarding the xz-trajectory, the vortices exhibit similar behavior for all variants. The trajectory distance to the wing surface decreases with increasing leading-edge radius. Primarily, the MBV of the large radius configuration is located closer to the wing surface.

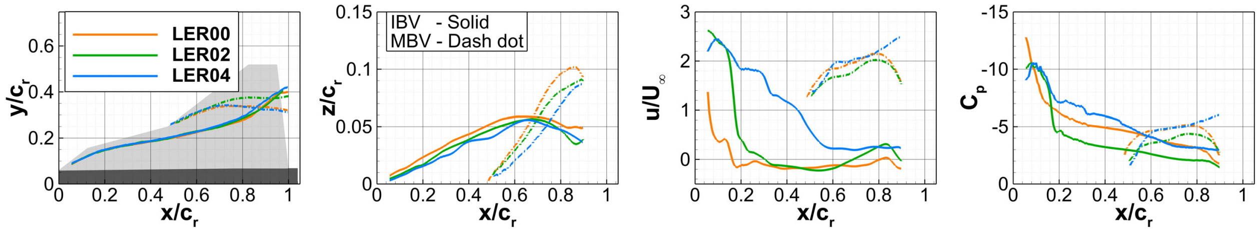

(a) y/c_r (b) z/c_r (c) u/U_∞ (d) C_P

Figure 6: Vortex core characteristics at $\alpha = 16°$ for the triple-delta-wing configuration.

Figure 6c presents the nondimensional axial core velocity. The variants with sharp and small radius leading edges indicate vortex breakdown by a rapid decrease in the axial IBV core velocity. The sharp-edged variant exhibits negative axial velocities in the core at $x/c_r \approx 0.18$ and the LER02 configuration at $x/c_r \approx 0.3$. Regarding the LER04 configuration, the decline in axial velocity is more gradual and even after breakdown, no negative axial velocities occur in the core. The MBV features a similar behavior for all variants; only in the rear part of the wing, the axial core velocity of the LER04 MBV increases. This can be attributed to the vortex interaction at the rear section of the wing and the vortex axis of the MBV oriented to the flow direction.

Accordingly, the vortex core pressure, cf. Fig. 6d, shows a rapid decrease in front of the wing section associated with vortex breakdown. In contrast to the axial velocity, the core pressure exhibits less differences between the variants. Especially the sharp-edged variant features a low pressure in the vortex , disregarding vortex breakdown and negative axial velocities in the core. In comparison to the double-delta-wing configuration, no direct interaction influence can be observed in the core pressure. Hence, no increase in core suction is shown.

7. Near-wall flow

The near-wall flow is analyzed in this chapter using the distribution of the surface pressure coefficient C_p and the wall-shear-stress lines, see Fig. 7. While converging streamlines indicate separation, diverging streamlines indicate reattachment, cf. Ref. [7]. The vortices induce a strong suction peak below the trajectory. This is well observable at the strake section of the double-delta-wing configuration. The higher the angle of attack, the broader and stronger the suction peaks become in correlation with the increasing rotational velocity of the vortices. At an angle of attack of $\alpha = 16°$, the strength of the suction peak at the strake decreases with increasing leading-edge radius.

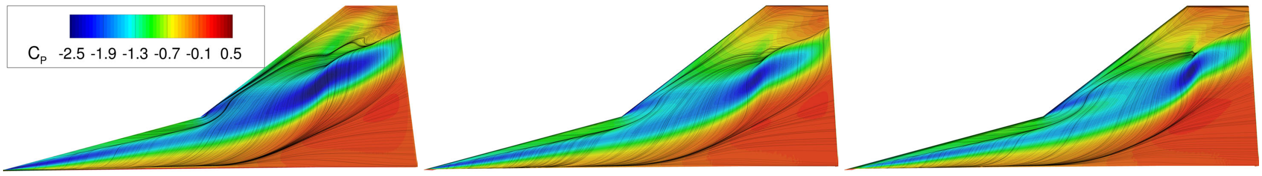

(a) LER00, $\alpha = 16°$ (b) LER02, $\alpha = 16°$ (c) LER04, $\alpha = 16°$

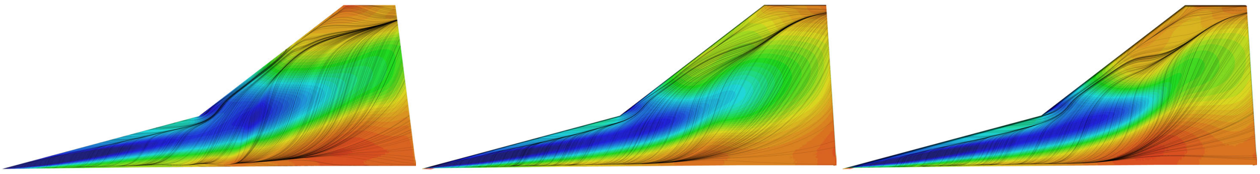

(d) LER00, $\alpha = 24°$ (e) LER02, $\alpha = 24°$ (f) LER04, $\alpha = 24°$

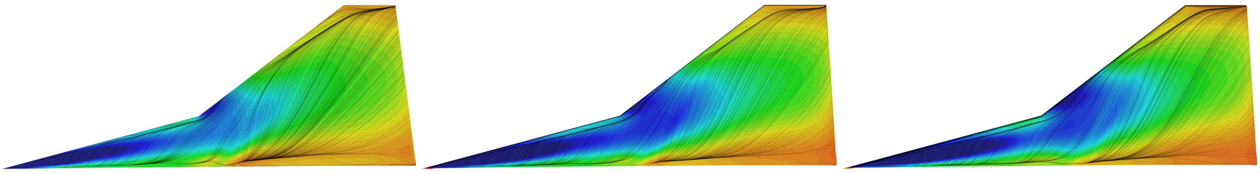

(g) LER00, $\alpha = 32°$ (h) LER02, $\alpha = 32°$ (i) LER04, $\alpha = 32°$

Figure 7: Surface pressure coefficient and wall shear stress lines for the double-delta-wing configuration.

All configurations exhibit a secondary separation between the suction peak and the leading edge at the strake section. The LER00 configuration also features the strongest suction downstream of the kink even though, as seen in Fig. 5, the vortices are located less close to the wing surface compared to the configurations with round leading edges. The reduced interaction is also visible due to the more separated suction peaks of the IBV and MBV downstream of the kink. Due to the delayed interaction of the vortices, the LER04 IBV exhibits more outboard deflection than the other configurations. The stronger and more linear trajectory of the intertwining vortices leads to an enhanced separation in the rear section of the wing of the LER00 configuration compared to the round leading-edge configurations. All configurations feature a prominent separation line in the rear of the wing. However, for the sharp-edged configuration, the suction in the outboard area is increased and the streamlines indicate reversed flow directly outboard of the separation line.

At an angle of attack of $\alpha = 24°$, see Figs. 7d to 7f, the increase in surface pressure at the main wing is a result of IBV breakdown. The sharp-edged configuration, cf. Fig. 7d, shows a broader area of pronounced suction area downstream of the kink as a consequence of the more upstream vortex breakdown occurring in an area where the MBV is developing and the forebody vortex is crossing the trajectories. The latter effect is observable due to an outboard-directed peak in the surface pressure distribution and abnormal distribution of the streamlines from the fuselage. For

DOI: 10.13009/EUCASS2023-418

the round-edged configurations, the more downstream located vortex breakdown leads to a more elongated, thinner, and stronger suction peak of the IBV. The MBV departs rapidly from the wing surface and does not show a prominent suction peak downstream of the kink.

With increasing angle of attack, the suction peaks increase and vortex breakdown occurs more upstream, resulting in a strong suction peak at the strake and a large wake area above the main wing. With increasing LER and increasing stability of the vortices, the suction peaks still occur more downstream and lead to a large suction area downstream of the kink enhanced by vortex-vortex interaction of IBV and MBV. This also results in a lower surface pressure coefficient close to the trailing edge for the LER02 and LER04 variants compared to the sharp-edged configuration. At this angle of attack, traces of a forebody vortex crossing appear for all configurations at a similar position.

The surface pressure coefficient distributions for the triple-delta-wing configuration are shown in Fig. 8. In the LEVCON section, a more pronounced suction peak occurs as a result of the lower leading-edge sweep compared to the double-delta-wing configuration. However, the suction peak decreases faster. At $\alpha = 16°$, see Figs. 8a to 8c, the LER00 and LER02 configurations show a quite similar surface pressure distribution with a slightly stronger IBV suction area for the sharp-edged variant. The configuration with the largest radius, see Fig. 4c, exhibits a pronounced MBV suction peak and an enhanced suction area close to the trailing edge as a result of IBV-MBV interaction. It also features a more pronounced secondary separation at the main wing close to the leading edge which is not observable for the LER00 and LER02 configurations.

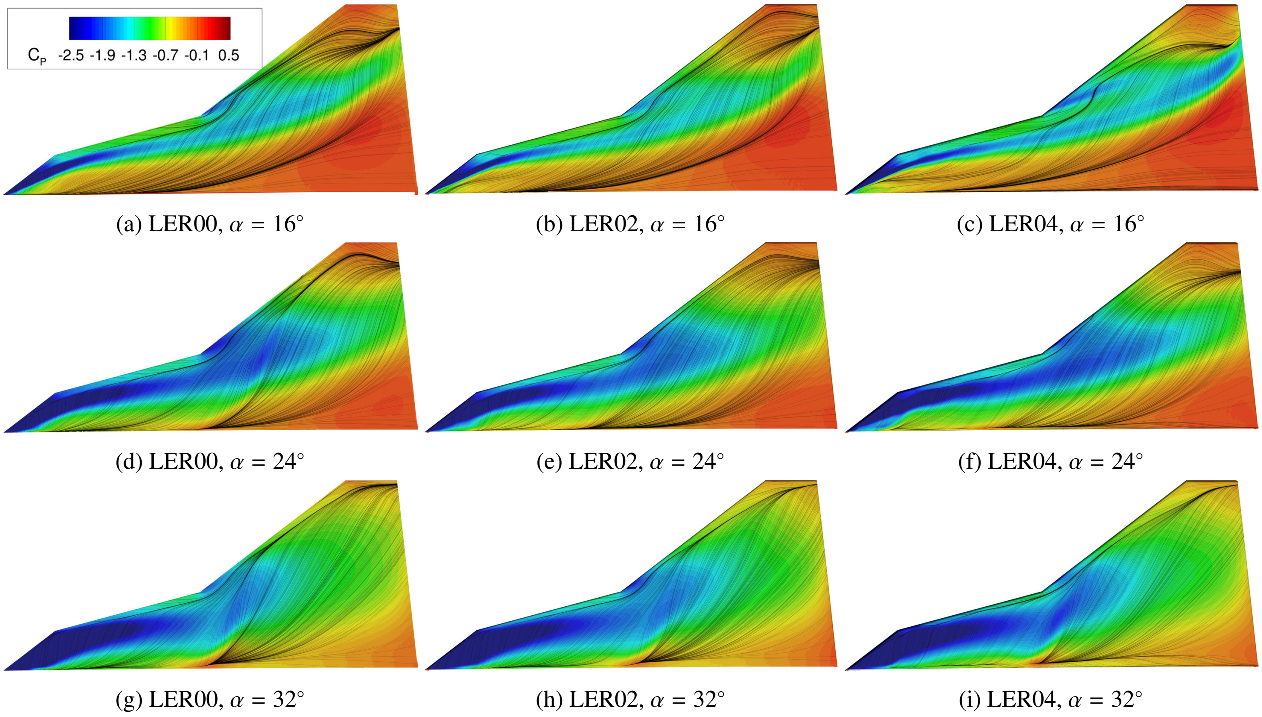

(a) LER00, $\alpha = 16°$ (b) LER02, $\alpha = 16°$ (c) LER04, $\alpha = 16°$

(d) LER00, $\alpha = 24°$ (e) LER02, $\alpha = 24°$ (f) LER04, $\alpha = 24°$

(g) LER00, $\alpha = 32°$ (h) LER02, $\alpha = 32°$ (i) LER04, $\alpha = 32°$

Figure 8: Surface pressure coefficient and wall shear stress lines for the triple-delta-wing configuration.

With an increase in the angle of attack to $\alpha = 24°$, see Figs. 8d to 8f, the breakdown of the vortex systems is observable by the pressure increase at the main wing. Similar to lower angles of attack and the double-delta-wing configuration, the LER04 configuration features a strong suction more downstream compared to the other configurations. The LER00 and LER02 configurations again exhibit quite similar behavior except for the indications for the forebody vortex crossing below the vortex system, which only occurs for the sharp-edged configuration.

At an angle of attack of $\alpha = 32°$, cf. Figs. 8g to 8i, a massive suction area occurs in the front section. This is observable until the main wing kink at $x/c_r = 0.475$, then decreases and is enhanced by the forebody vortex crossing at all configurations.

8. Stability Characteristics

The global coefficients of the force and moment measurements and the simulations are discussed in this section for symmetric and only experimental results for asymmetric, $\beta = 5°$, freestream conditions. The global coefficients for the double-delta-wing configurations are shown in Fig. 9. The sharp-edged configuration is represented by an orange line and square symbols, the LER02 variant by a green line and triangle symbols, and the large radius configuration is illustrated by a blue line and diamond-shaped symbols. Experimental data is depicted by lines and numerical data by symbols. The lift and pitching moment coefficients at no angle of sideslip are shown in Fig. 9a. The pitching moment coefficient is visually distinguished from the lift coefficient by a dashed-dot line and white-filled symbols. The CFD results feature a decrease in lift at lower angles of attack for all configurations. The LER04 configuration exhibits the best agreement with experimental data compared to the other variants. The pitching moment coefficient also is in good agreement with the experiments except for the pitch-up tendency at lower angles of attack.

In the experimental results, the LER04 configuration exhibits a slightly lower lift increase at medium angles of attack, $9^\circ < \alpha < 22^\circ$ compared to the sharp-edged and small-radius variants. At an angle of attack of $\alpha = 23^\circ$ for LER00, $\alpha = 24^\circ$ for LER02, and $\alpha = 22^\circ$ for LER04 configuration, the lift decreases and the pitching moment increases. This is a result of an abrupt upstream shift of vortex breakdown.

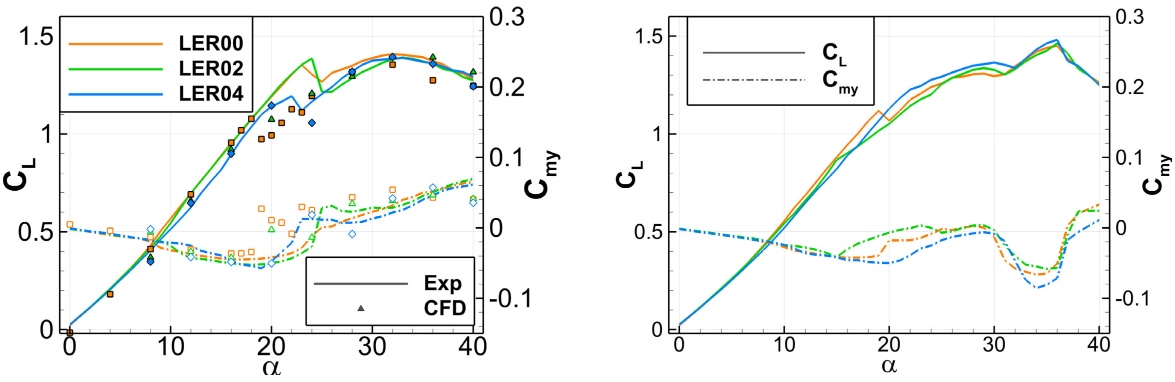

(a) Longitudinal coefficients at $\beta = 0^\circ$

(b) Longitudinal coefficients at $\beta = 5^\circ$

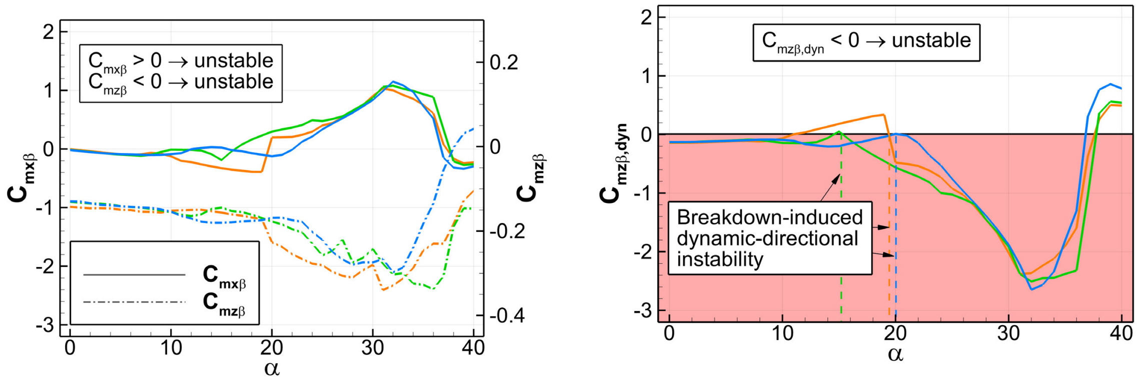

(c) Lateral coefficients at $\beta = 5^\circ$

(d) Dynamic directional stability coefficient $C_{mz,dyn}$ at $\beta = 5^\circ$

Figure 9: Global coefficients for the double-delta-wing configuration.

For the LER02 configuration, the lift decrease is the highest and most abrupt between the configurations. The configuration with the highest leading-edge radius features lower maximum lift in the region $20^\circ < \alpha < 25^\circ$. The lift and pitching moments polars of the different variants converge for higher angles of attack.

For a sideslip angle, the longitudinal stability characteristics are shown in Fig. 9b. The most interesting angle of attack section is between $14^\circ < \alpha < 25^\circ$. At $\alpha \approx 14^\circ$, the LER02 configuration exhibits a slight lift decrease and pitching moment increase, indicating vortex breakdown. The LER00 variant features a drop in lift coefficient at $\alpha \approx 19^\circ$. However, the LER04 configuration shows no drop in lift and the pitching moment coefficient increases gradually from $\alpha \approx 21^\circ$. Still, a lower $C_{L,\alpha}$ increase at lower angles of attack, $\alpha < 18^\circ$, is observable. At higher angles of attack $\alpha > 25^\circ$ the configurations feature a similar behavior.

The lateral stability characteristics are discussed by means of the lateral, $C_{mx\beta}$, the directional, $C_{mz\beta}$, and the dynamic directional stability, $C_{mz\beta,dyn}$. The first are the derivatives of the rolling and yawing moment coefficient, respectively. The lateral stability parameter represented by solid lines and filled symbols shows a neutral-stable behavior up to an angle of attack of $\alpha \approx 19^\circ$ for LER00, $\alpha \approx 16^\circ$ for LER02, and $\alpha \approx 23^\circ$ for LER04 variant. These coincide

DOI: 10.13009/EUCASS2023-418

well with the previously mentioned critical angles of attack observed in the longitudinal stability characteristics. With a further increase in angle of attack, the rolling moment coefficient increases in the unstable region up to $\alpha \approx 32°$. For even higher angles of attack, the vortex breakdown moves upstream at the leeward side, resulting in a more symmetric flow field on both wings and, therefore, a decrease in rolling moment coefficient. Due to the lack of tail/fin surfaces, the directional stability parameter exhibits an unstable behavior for the whole range of angles of incidence. This also influences the dynamic directional stability but the values for $\alpha < 16°$ are in the region of neutral stability. For higher angles of attack, a breakdown-induced dynamic directional instability occurs. This results from a one-sided, at the windward side, vortex breakdown while the other side features a stable vortex system. The LER00 variant exhibits the most abrupt and, therefore, most critical rolling moment reversal leading not only to lateral instability but also to directional as well as dynamic directional instability.

The longitudinal and lateral stability characteristics for the triple-delta-wing configuration are shown in Fig. 10. At $\beta = 0°$, cf. Fig. 10a, the lift coefficient exhibits almost no sensitivity to the LER. The computational results are in good agreement with the experimental data for angles of attack of $\alpha < 32°$ for all variants. For higher angles of attack, the results diverge especially regarding the pitching moment coefficient. In the experimental results, all configurations show similar lift coefficient polars. Regarding the pitching moment coefficient, the variants with round leading edges exhibit an increase at higher angles of attack due to later vortex breakdown. The pitching moment derivative increases significantly beyond $\alpha \approx 12°$ for LER00 configuration and beyond $\alpha \approx 15°$ for the round leading-edge variants. It is observable that the LER02 configuration features a slightly higher pitching moment derivative in the region of $15° < \alpha < 25°$ compared to the LER04 variant. Similar to the double-delta-wing configuration, the C_L and C_{my} characteristics of all variants converge for higher angles of attack. The same characteristics can be observed for the longitudinal stability parameters at an angle of sideslip of $\beta = 5°$.

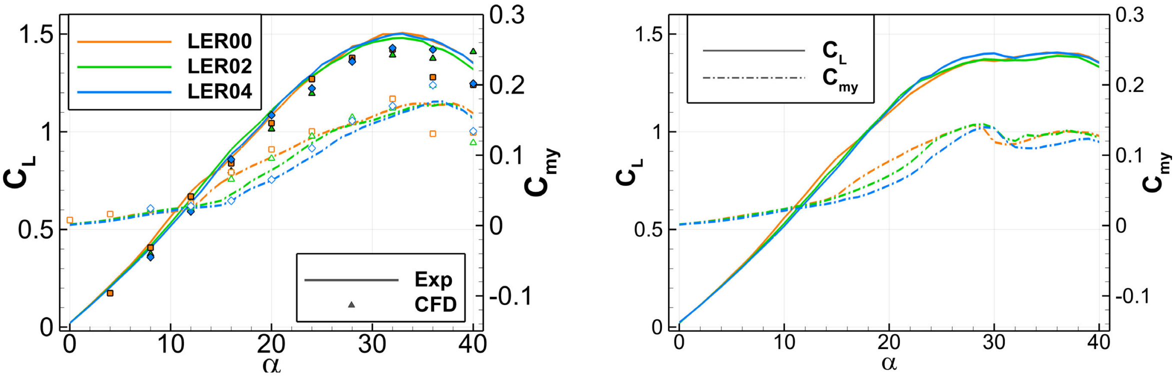

(a) Longitudinal coefficients at $\beta = 0°$

(b) Longitudinal coefficients at $\beta = 5°$

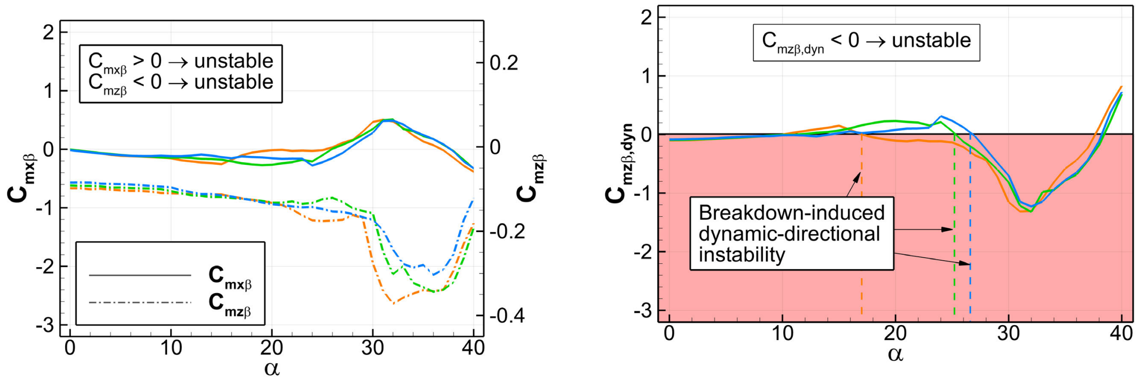

(c) Lateral coefficients at $\beta = 5°$

(d) Dynamic directional stability coefficient $C_{mz,dyn}$ at $\beta = 5°$

Figure 10: Global coefficients for the triple-delta-wing configuration.

The lateral stability characteristics are shown in Figs. 10c and 10d. Similar to the double-delta-wing configuration, the directional stability parameter $C_{mz\beta}$ shows an unstable behavior over the whole wing. While the rolling moment coefficient exhibits a stable behavior up to $\alpha \approx 27°$ for the LER00 and LER02 variants and $\alpha \approx 28°$ for the LER04 configuration, the dynamic stability parameter shows an unstable behavior at lower angles of attack. For this

DOI: 10.13009/EUCASS2023-418

parameter, the sharp-edged configuration behaves unstable from $\alpha \approx 17^\circ$, but low values of the dynamic directional stability parameter indicate a rather neutral stable behavior.

The increase in leading-edge radius slightly stabilizes the flight mechanical characteristics at asymmetric freestream conditions. However, the triple-delta-wing configuration features less sensitivity to the LER influence on the stability characteristics than the double-delta-wing configuration. The developing vortex system is susceptible to geometrical and freestream changes for the latter. This sensitivity is limited to an angle of attack range of $20^\circ < \alpha < 26^\circ$ and $15^\circ < \alpha < 24^\circ$ regarding the symmetric freestream case and the one at an angle of sideslip of $\beta = 5^\circ$, respectively.

9. Conclusion and Outlook

This study conducted extensive wind tunnel experiments and simulations to analyze the influence of the leading-edge radius on a vortex system developing at hybrid-delta-wing configurations. Two variants with leading-edge radii of $r_N/c_r = 0.0025$ and $r_N/c_r = 0.005$ are investigated and compared to the results of a sharp-edged configuration. The simulations were conducted with the DLR-TAU code and are the basis for the flow field, vortex core, and near-wall flow analysis. The flow field is analyzed at distinct angles of attack $\alpha = \{16^\circ, 24^\circ, 32^\circ\}$ at symmetric freestream conditions. For the vortex core analysis, an angle of attack of $\alpha = 16^\circ$ is chosen due to the vortices' strong interaction and best comparability without vortex breakdown. The experimental force and moment results are shown at an angle of sideslip of $\beta = 0^\circ$ and $\beta = 5^\circ$.

The results show a similar vortex development at the given angles of attack for both configurations. For the double-delta-wing configuration, the strake vortex features higher stability at high angles of attack. This is indicated by a downstream delay of the vortex breakdown with increasing LER and angle of attack. Similar to the more downstream vortex breakdown for increasing LER, it can be shown that the interaction of the vortices occurs more downstream. Therefore, a weaker attraction between the vortices is implied. This weaker attraction also influences the trajectory of the forebody vortex, which is only observable at the sharp-edged configuration. The interaction of the vortices induces an increase in suction and axial velocity in the vortex core. This can be associated with an increased suction and velocity level in the vortex core of the configuration with a sharp leading edge compared to the round-edged variants. The force and moment measurements show that the vortex system is sensitive to leading-edge changes at medium to high angles of attack in a range of $14^\circ < \alpha < 25^\circ$ for symmetric and asymmetric freestream conditions. In this range, the vortices become more unstable and slight changes can lead to a more upstream or more downstream vortex breakdown. At an angle of sideslip of $\beta = 5^\circ$, the moment coefficients indicate a more gradual vortex breakdown at configurations with round leading edges.

For the triple-delta-wing configuration, the influence of the leading-edge radius is lower compared to the double-delta-wing configuration. The flow fields of the configurations with different leading-edge radii are similar. In the vortex core analysis, the stabilization of the strake vortex due to the larger leading-edge radius is shown. Regarding the vortex interaction, the sharp-edged and the medium variants exhibit quite similar vortex trajectories. However, the configuration with the large leading-edge radius features no inboard movement of the MBV. Additionally, the suction peak of the strake vortex of the latter is stronger and intensifies close to the trailing edge due to the delayed vortex interaction. Furthermore, the pitching moment coefficient indicates a vortex breakdown above the wing at slightly higher angles of attack with increasing leading-edge radius. The dynamic directional stability parameter indicates a similar flight behavior for all variants. Only a slight increase in stability occurs for larger leading-edge radius, but all variants are the region of neutral stability up to $\alpha \approx 26^\circ$.

These results confirm the less sensitive flow fields and less critical flight mechanical behavior of the triple-delta-wing configuration compared to the double-delta-wing configuration. Both configuration types feature a more stable strake vortex and similar MBV development between the variants. For a better understanding of the vortices and their influence on the flight mechanical behavior, an analysis of the attraction between the vortices and of the stabilizing and destabilizing effects of the vortex interaction is of great importance.

Acknowledgments

The Deutsche Forschungsgemeinschaft (DFG, German Research Foundation) funded the project - grant number BR1511/13-2. The fruitful cooperation with Airbus Defense and Space and the German Aerospace Center (DLR), especially within the framework of the NATO STO AVT316, is gratefully acknowledged. Furthermore, the authors thank the German Aerospace Center (DLR) for providing the DLR TAU-Code used for the numerical investigations and Michael Werner for developing the vortex tracing algorithm. Moreover, the authors gratefully acknowledge the Gauss Centre for Supercomputing e.V. (http://www.gauss-centre.eu) for funding this project by providing computing time on the GCS Supercomputer SuperMUC at Leibniz Supercomputing Centre (http://www.lrz.de). The authors also highly appreciate the previous wind tunnel tests by Stefan Pfnür.

DOI: 10.13009/EUCASS2023-418

References

[1] Hitzel, S.: Sub- and Transonic Vortex Breakdown Flight Condition Simulations of the F-16XL Aircraft. Journal of Aircraft **31**(4), 868–878 (2016). `https://doi.org/10.2514/3.46573`

[2] Hummel, D., John, H., Staudacher, W.: Aerodynamic Characteristics of Wing-Body-Combinations at High Angles of Attack. In: 14th Congress of the International Council of the Aeronautical Sciences, International Council of the Aeronautical Sciences Paper 2.7.1, Amsterdam, Netherlands,, pp. 747–762 (1984)

[3] Breitsamter, C.: Unsteady flow phenomena associated with leading-edge vortices. Progress in Aerospace Sciences **44**(1), 48–65 (2008). `https://doi.org/10.1016/j.paerosci.2007.10.002`

[4] Gursul, I.: Review of Unsteady Vortex Flows over Slender Delta Wings. Journal of Aircraft **42**(2), 299–319 (2005). `https://doi.org/10.2514/1.5269`

[5] Brennenstuhl, U., Hummel, D.: Vortex Formation over Double-Delta Wings. 13th Congress of the International Council of the Aeronautical Sciences, International Council of the Aeronautical Sciences Paper 6.6.3, Amsterdam, The Netherlands,, 1133–1146 (1982)

[6] Pfnür, S., Breitsamter, C.: Stereo-PIV Measurements of Vortex-Interaction Effects on Generic Delta Wing Planforms. In: 13th International Symposium on Particle Image Velocimetry – ISPIV 2019 (2019)

[7] Sedlacek, D., Biechele, S., Breitsamter, C.: Numerical investigations of vortex formation on a generic multiple-swept-wing configuration. CEAS Aeronautical Journal (2021). `https://doi.org/10.1007/s13272-021-00566-y`

[8] Sedlacek, D., Breitsamter, C.: Aerodynamic characteristics and topology of interfering vortex systems at hybrid-delta wings. Journal of Aircraft, 1–17 (2022) https://doi.org/10.2514/1.C036947. `https://doi.org/10.2514/1.C036947`

[9] Pfnür, S., Breitsamter, C.: Leading-Edge Vortex Interactions at a Generic Multiple Swept-Wing Aircraft Configuration. Journal of Aircraft **56**(6), 2093–2107 (2019). `https://doi.org/10.2514/1.C035491`

[10] Spalart, P., Allmaras, S.: A One-equation Turbulence Model for Aerodynamic Flows. In: 30th Aerospace Sciences Meeting and Exhibit (1992). `https://doi.org/10.2514/6.1992-439`

[11] Shur, M.L., Spalart, P.R.: On the Sensitization of Turbulence Models to Rotation and Curvature. AIAA Journal **38**(5), 784–792 (1997). `https://doi.org/10.2514/2.1058`

[12] Morton, S., Forsythe, J., Mitchel, A., Hajek, D.: DES and RANS Simulations of Delta Wing Vortical Flows. AIAA 2002-0587 (2002). `https://doi.org/10.2514/6.2002-587`

[13] Luckring, J.M., Park, M.A., Hitzel, S.M., Jirásek, A., Lofthouse, A.J., Morton, S.A., McDaniel, D.R., Rizzi, A., Tomac, M.: Synthesis of hybrid computational fluid dynamics results for f-16xl aircraft aerodynamics. Journal of Aircraft **54**(6), 2100–2114 (2017). `https://doi.org/10.2514/1.C034053`

[14] Luckring, J.M.: Reynolds Number, Compressibility and Leading-Edge Bluntness Effects on Delta-Wing Aerodynamics. In: 24th International Congress of the Aeronautical Sciences (2004)

[15] Cummings, R.M., Morton, S.A., McDaniel, D.R.: Experiences in accurately predicting time-dependent flows. Progress in Aerospace Sciences **44**(4), 241–257 (2008). `https://doi.org/10.1016/j.paerosci.2008.01.001`

[16] Allmaras, S., Johnson, F., Spalart, P.: Modifications and Clarifications for the Implementation of the Spalart-Allmaras Turbulence Model. Seventh International Conference on Computational Fluid Dynamics (ICCFD7) (2012)

[17] Shur, M.L., Strelets, M.K., Travin, A.K., Spalart, P.R.: Turbulence Modeling in Rotating and Curved Channels: Assessing the Spalart-Shur Correction. AIAA Journal **38**(5), 784–792 (2000). `https://doi.org/10.2514/2.1058`

[18] Frink, N., Tomac, M., Rizzi, A.: Collaborative Study of Incipient Separation on 53deg Swept Diamond Wing. Aerospace Science and Technology **57**, 76–89 (2016)

[19] Kolář, V.: Vortex identification: New requirements and limitations. International Journal of Heat and Fluid Flow **28**(4), 638–652 (2007). `https://doi.org/10.1016/j.ijheatfluidflow.2007.03.004`